NANO LETTERS

pubs.acs.org/NanoLett Letter

Multidimensional Image and Beam Splitter Based on Hyperbolic Metamaterials

Sha Hu, Shuo Du, Junjie Li, and Changzhi Gu*

Cite This: https://dx.doi.org/10.1021/acs.nanolett.0c04795 Read Online

ACCESS | Metrics & More | Article Recommendations | Supporting Information

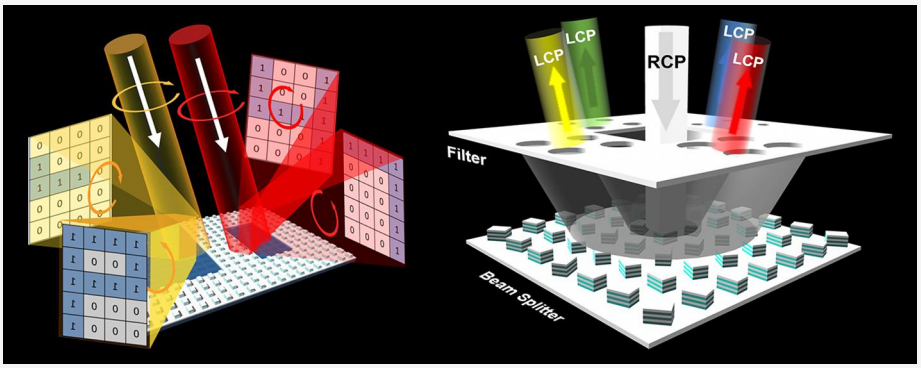

ABSTRACT: Recently, multidimensional metasurfaces, which can modulate multiple optical parameters of input and output lights simultaneously, have aroused intensive interest. Here, we demonstrate multidimensional switchable images and 3D integrated beam splitters based on hyperbolic metamaterials (HMMs). On one hand, a switchable image controlled by output helicity and input wavelengths is achieved by arranging HMMs with different polarization conversion performance. On the other hand, polarization-multiplexed broadband beam splitter is generated by spatially engineering the subunit with broadband half-plate performance. By integrating the multiplexed beam splitter with a filter metamaterial, this multidimensional beam splitter can further realize the separation of output light by space and wavelength. This cascaded multilayer metamaterial achieves a brand new optical functionality and offers more inspiring possibilities for the design of multifunctional optical devices in the future.

KEYWORDS: *Hyperbolic metamaterials, Multidimensional control, Switchable image, Beam splitter*

The spatially inhomogeneous metasurface was first demonstrated by Cappaso's group in 2011,[1] which introduced a phase coverage of 2π and provided full wavefront control. Subsequently, various wavefront shaping phenomena have been extensively studied based on resonant phase metasurfaces.[2−4] However, the resonant phases are sensitively dependent on delicate control of the geometric parameters, thus leading to complex design, high accuracy, and narrow bandwidth.[5−7] Recently, Pancharatnam−Berry (PB) phase φ (namely geometric phase), which is determined by orientation angle θ of building blocks ($\varphi = \pm 2\theta$),[8,9] has been extensively studied to overcome the limitation of narrow bandwidth.[10] The geometric phase is attached to the cross-polarized component of circularly polarized incident light.[11−13] Therefore, broadband circular polarization conversion is a prerequisite for broadband wavefront manipulation of geometric metasurfaces. In recent years, hyperbolic metamaterials (HMMs) have been widely studied in order to achieve birefringence and circular polarization conversion in a wide band.[14,15] For example, HMMs are proposed to generate broadband Airy beams by taking advantage of the broadband and high birefringence in the microwave/infrared regimes.[16] Broadband wavefront manipulation based on HMMs is rarely demonstrated in the visible range.

To dramatically extend the applications of metamaterial, multidimensional functionalities have increasingly become the focus of metamaterial development. On one hand, by controlling the single optical parameter of light, various multiplexed metasurfaces have been demonstrated, such as multiwavelength metalens,[17,18] helicity multiplexed holograms,[19,20] and the generator of an arbitrary combination of polarization states.[21] On the other hand, based on the simultaneous control of multiple optical parameters of input and output lights, some striking optical devices are generated, such as color holographic imaging[22−24] and a focusing lens combined with a waveplate.[25]

Received: December 4, 2020
Revised: February 6, 2021

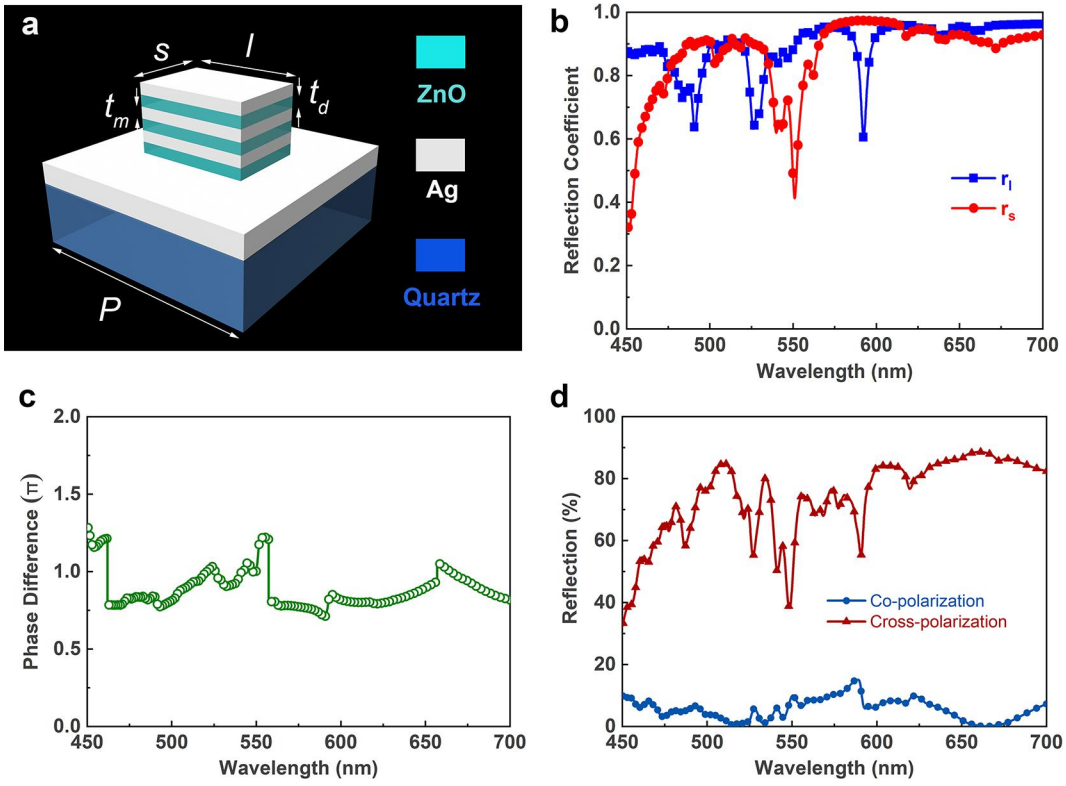

Figure 1. HMMs composed of stacked Ag and ZnO nanosheets. (a) Schematic of the unit cell of HMMs. This multilayer structure consists of three pairs of Ag−ZnO nanosheets with period P = 400 nm, length of long axis l = 220 nm, and length of short axis s = 115 nm. t_d = 25 nm and t_m = 35 nm denote the thickness of ZnO and Ag nanosheets, respectively. (b) Reflection coefficient and (c) phase difference of the HMM when incident light is polarized along the long and short axes of nanosheets, respectively. (d) Cross-polarization and copolarization reflectivity under normal incidence with circular polarization.

In this Letter, a ZnO-Ag-stacked HMM is proposed to realize multidimensional control of light by taking advantages of the broadband birefringence and geometric phase modulation in the visible range. By adjusting the geometric parameters, HMMs with different circular polarization conversion performance are obtained. On the basis of this, a multiplexed switchable image controlled by incident wavelength and reflection polarization is demonstrated. By introducing geometric phase into the HMMs, a polarization-multiplexed broadband circular beam splitter can be realized. Furthermore, a 3D integrated metamaterial, which is designed by stacking the multiplexed beam splitter with a multi-wavelength filter, can simultaneously fulfill circular polarization conversion and prism functions. This integrated metamaterial can realize simultaneous control of input and output optical parameters and achieve a novel optical functionality in microscale.

RESULTS AND DISCUSSION

We demonstrate a broadband circular polarization converter based on HMMs, which consists of stacked blocks with a three pairs of Ag−ZnO nanosheets on a ground metal plane, as depicted in Figure 1a. The unit cell is with the length of long axis l = 220 nm and the length of long axis s = 115 nm. These unit cells are arranged with period P = 400 nm. The thickness of ZnO and Ag nanosheets are t_d = 25 nm and t_m = 35 nm, respectively. The ground metal plane is a silver film with a thickness of 100 nm on the quartz substrate. Under linearly polarized incidence, the Jones matrix $\mathbf{R}_{lin}$ of HMMs can be expressed as

$$\mathbf{R}_{lin} = \begin{pmatrix} r_l & 0 \\ 0 & r_s e^{i\Delta\varphi} \end{pmatrix} \tag{1}$$

where r_l and r_s denote the reflection coefficients of the HMM for incident linear polarization along the long and short axes of nanosheets, respectively, and $\Delta\varphi$ presents the phase retardation between the orthogonal long and short axes. By changing the Cartesian base to circular base, the Jones matrix $\mathbf{R}_{circ}$ can be derived

$$\mathbf{R}_{circ} = \begin{pmatrix} R_{RR} & R_{RL} \\ R_{LR} & R_{LL} \end{pmatrix} = \frac{1}{2}\begin{pmatrix} r_l + r_s e^{i\Delta\varphi} & r_l - r_s e^{i\Delta\varphi} \\ r_l - r_s e^{i\Delta\varphi} & r_l + r_s e^{i\Delta\varphi} \end{pmatrix} \tag{2}$$

where R_{ij} $(i, j = R, L)$ represents the ratio of the complex amplitude of i-circularly polarized reflected wave to that of j-circularly polarized incident light. The copolarization (r_{RR}) and cross-polarization (r_{LR}) components of reflected light can be described as

$$\begin{cases} r_{RR} = |R_{RR}|^2 = \frac{1}{4}|r_l + r_s e^{i\Delta\varphi}|^2 \\ r_{LR} = |R_{LR}|^2 = \frac{1}{4}|r_l - r_s e^{i\Delta\varphi}|^2 \end{cases} \tag{3}$$

Therefore, complete conversion between two orthogonal circular polarization states could be realized under particular conditions with $r_l = r_s$ and $\Delta\varphi = \pi$.

Numerical simulations are performed by using the frequency domain solver of the software CST Microwave Studio. In the

https://dx.doi.org/10.1021/acs.nanolett.0c04795
Nano Lett. XXXX, XXX, XXX−XXX

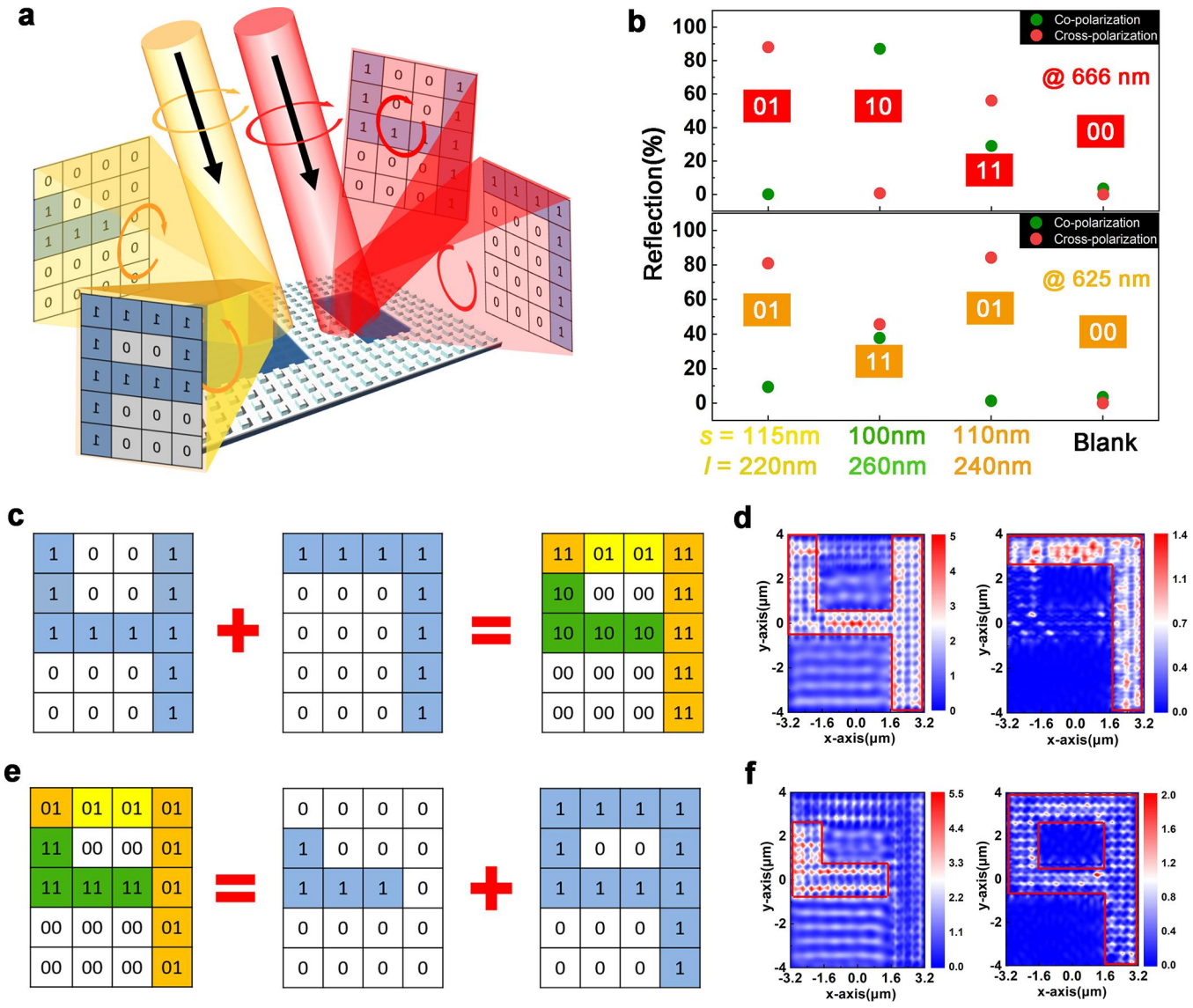

Figure 2. Switchable image controlled by input wavelength and output polarization. (a) The schematic diagram of switching image. (b) Copolarization and cross-polarization reflectivity of four selected HMMs with different geometrical sizes at incident wavelengths of 666 and 625 nm, respectively. (c) The design of switching image at 666 nm: the left and middle patterns are the images controlled by copolarization and cross-polarization components (number "4" and "7"), respectively, and the right pattern is overlapped by "4" and "7" which determines the arrangement of multiplexed image. (d) Simulated electric field distributions for RCP-component distribution (left) and LCP-component distribution (right) at the incident wavelength of 666 nm. (e) The left pattern designed in (c) can be decoded to the middle pattern (detected by RCP analyzer) and right pattern (detected LCP analyzer) under RCP irradiation at 625 nm. (f) Simulated electric field distributions at 625 nm: RCP-component distribution (left) and LCP-component distribution (right), respectively.

simulation, the permittivities of ZnO and Ag are both extracted from ellipsometric measurements. Periodic boundary conditions on both x- and y-directions are applied to characterize the periodic structure, and an open boundary is imposed in the z-direction. On one hand, the reflection coefficient r_l and r_s are both high and close to each other over a brand waveband, as the simulated results in Figure 1b show. There exist several falls in the r_l and r_s spectra, which result from the absorption modes in HMMs (see the Supporting Information for details). On the other hand, phase differences of the HMM along two orthogonal directions approach π in a wide wavelength band of 450−700 nm. Hence, high conversion between two orthogonal circular polarization states can be produced in a wide band. As the copolarization and cross-polarization reflection spectrum indicate, the desired cross-polarization reflection is averagely higher than 60%, while the unwanted copolarization light can be suppressed to below 10%.

The above analysis indicates that the reflected polarization state of HMMs has close dependency on geometric parameters as well as incident wavelength. On the basis of this, a switchable image controlled by input wavelength and output polarization can be designed by arranging HMMs with different polarization conversion performance, as Figure 2a illustrates. We carefully select four HMMs with different geometrical sizes as pixels of designed switchable image. Figure 2b provides the copolarization and cross-polarization reflectivity of the four pixels at incident wavelengths of 666 and 625 nm, respectively. Because the circular polarization conversion of proposed anisotropic HMM is independent of the helicity of incident light, only right-circularly polarized (RCP) incident

https://dx.doi.org/10.1021/acs.nanolett.0c04795
Nano Lett. XXXX, XXX, XXX−XXX

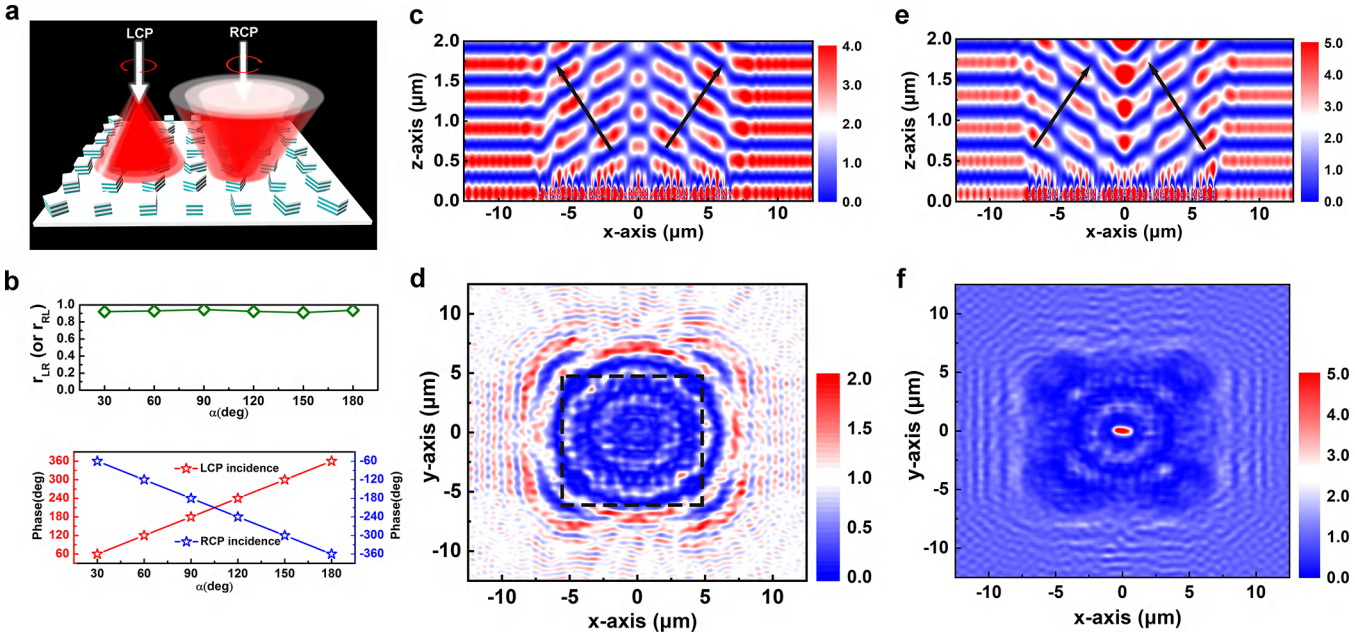

Figure 3. Broadband circular polarization beam splitter with input polarization multiplexing. (a) Schematic of beam splitter under RCP and LCP incidences, respectively. (b) Cross-polarization reflectivity (r_{RL} or r_{LR}) and geometric phase of structure 1 with different rotation angles. The electric field distributions in (c) $x-z$ plane and (d) $x-y$ plane under RCP irradiation at 666 nm, respectively. The electric field distributions in (e) $x-z$ plane and (f) $x-y$ plane under LCP irradiation at 666 nm, respectively.

light is applied for simplicity. For RCP incidence at 666 nm, the reflected polarization helicity of the four HMMs is significantly different. The reflected light of structure 1 (s = 115 nm, l = 220 nm) only has the cross-polarization (left-circularly polarized, LCP) component. Conversely, the reflected light of structure 2 (s = 100 nm, l = 260 nm) only has the copolarization component, namely RCP component. Besides, the reflected light of structure 3 (s = 110 nm, l = 240 nm) contains both LCP and RCP components. The blank structure in Figure 2b refers to the quartz substrate without HMM nanostructures or Ag backplane (structure 4), which barely has reflected light. The output polarization components of those nanostructures can be represented by "0" and "1" when the reflected light passes through RCP and LCP analyzers (see the Supporting Information for details). Therefore, 2-bit coding is constructed by a sequence of four coding pixels "00", "01", "10", and "11", as Figure 2b presents. By arranging coding pixels, we propose a switchable metamaterial image controlled by output polarization helicity, as illustrated in Figure 2c. The designed image shows the number "4" for reflected RCP component while the image displays the number "7" with the helicity of reflected light switching to LCP. Combining the two switched images, we receive the arrangement of this switching metamaterial, as schematically shown in the right pattern of Figure 2c.

FDTD solutions software is used to verify the feasibility of the polarization-controlled switching image. In the simulation, each color patch in Figure 2c is composed of 4 × 4 units, and the image is illuminated under RCP light at a wavelength of 666 nm along the z-direction. The monitors are set above the light source to detect the electric field distributions of the proposed image. A resolution of ∼15 800 dpi can be achieved for our switchable images. The electric field distributions of RCP and LCP components illustrated in Figure 2d obviously show the number "4" and "7", respectively. This indicates that the electric field distributions for different circular polarization components are consistent with the switchable images under different analyzers. Therefore, a switchable display controlled by output helicity can be realized by rationally arranging the structures with different circular polarization conversion performance.

In addition, there is a further attention that the reflected polarization states of HMMs are subject to dispersion. Therefore, the reflectivity and PCR values of corresponding pixels in Figure 2b will change as incident wavelength varies. Taking the incident wavelength of 625 nm as an instance (see the bottom part of Figure 2b), structure 1 keeps the same high-efficiency polarization conversion as before: the RCP component is "0" and the LCP component is "1". For structure 2, its reflection state changes: the RCP and LCP components are equivalent, which are both represented as "1". The new reflection state of structure 3 is similar to that of structure 1: RCP component is "0" while LCP component is "1". The reflection components of structure 4 remain unchanged. When the incident wavelength switches to 625 nm, the change of reflected polarization states of pixels will result in a new image display. That is to say, the switching image is wavelength multiplexed. When the switching image is decoded under RCP and LCP analyzers, we can obtain different displays as the middle and right patterns of Figure 2e illustrate. The electric field distributions in Figure 2f indicate that the electric field distribution of the copolarized (RCP) component shows the shape of a short "L" while that of the cross-polarized (LCP) component is similar to the number "9". It implies that the simulated electric field distributions have the same displays as the decoded patterns. Significantly, when the incident wavelength changes again, the displayed image changes correspondingly. In addition, the switchable images show different colors as the incident wavelength changes. Consequently, this multiplexed image based on HMM can realize the switch of displayed patterns under different optical parameters and achieve multifunctional optical encryption.

https://dx.doi.org/10.1021/acs.nanolett.0c04795
Nano Lett. XXXX, XXX, XXX−XXX

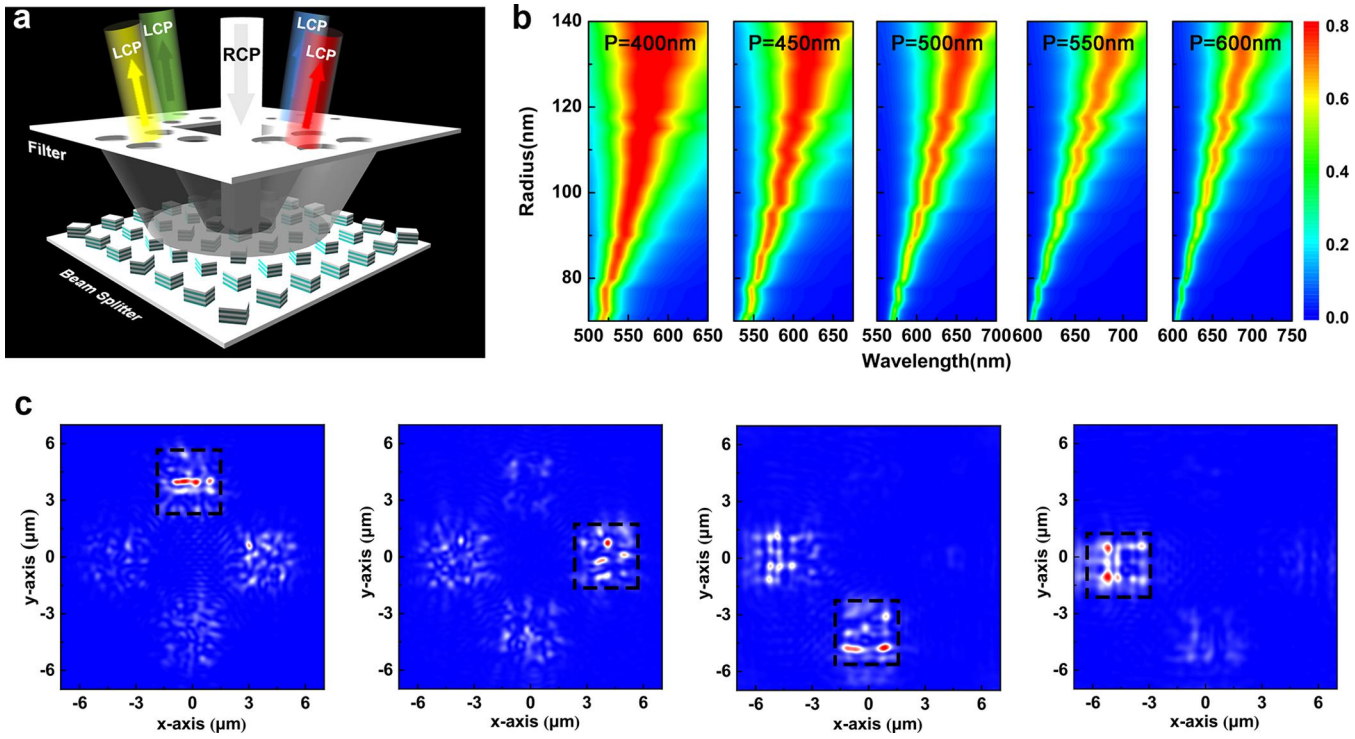

Figure 4. Multidimensional beam splitter based on a 3D-integrated metamaterial. (a) Schematic of the designed 3D-integrated metamaterial by vertically stacking a filter metamaterial with the broadband beam splitter. (b) The simulated transmission spectra of filter metamaterials under different periods (P) and radii. (c) The simulated electric field distributions in $x-y$ plane for 3D integrated metamaterial under different incident wavelengths: 529, 569, 635, and 675 nm, respectively.

It is worth noting that the proposed HMMs can realize broadband and high polarization conversion by properly designing the geometric parameters, such as structure 1. On the basis of this, we demonstrate a broadband circular beam splitter by spatially rotating structure 1 and introducing desired geometric phase distributions, as Figure 3a shows. The beam splitter based on geometric metasurface essentially results from an anomalous deflection phenomenon based on the generalized Snell's law. In detail, the copolarized component does not possess phase gradient and follows the conventional reflection law while the cross-polarized component introduces a discontinuous phase distribution and leads to anomalous reflection. As illustrated in Figure 3a, the reflected light from the beam splitter is an inverted cone under RCP illumination, whereas, the reflected light is concentrated toward the z-axis of designed splitter when LCP light is incident. It is well-known that linearly polarized light can be regarded as the superposition of LCP and RCP lights with the same frequency, amplitude, phase, and propagation direction. Therefore, when the beam splitter is irradiated by linearly polarized light, the LCP component is concentrated toward the central axis while the RCP component flows outward, thus resulting in circular polarization beam splitting. Here, we choose the structure 1 (l = 220 nm and s = 115 nm) as the subunit of the splitter. The subunits are arranged with the rotation angle gradient $\alpha(x, y) = \pi r/P_r$, where the rotation step is 30° ($P_r = 6P$) and $r = x + y$ is the distance of the subunit from the metasurface center (see Supporting Information). The subunits on the concentric circle have the same rotation angle. Besides, the complete phase coverage 2π can be achieved along the radial direction (Figure 3b). Meanwhile, the reflection intensity of cross-polarized light remains uniform for the subunits with different rotation angles. Figure 3c,d shows the electric field distributions in the $x-z$ and $x-y$ planes with RCP incidence at 666 nm, respectively. The electric field distributions in the $x-z$ plane indicate that the reflected cross-polarized light flows outward with a certain angle. The $x-y$ plane in Figure 3d is suspended at 5 μm above the beam splitter and the dotted line represents the boundary of this splitter. The electric field distributions in the $x-y$ plane also reveal that the reflection spreads out. The angle of beam deflection calculated from the electric field distribution is 16.1°, which is consistent with that calculated by the generalized Snell's law (see Supporting Information).

For LCP and RCP incidences, the space-variant metasurface holds the opposite sign of geometric phase gradients, leading to different far-field intensity distributions. When the incident wave is switched to LCP illumination, the electric field distributions in the $x-z$ plane and $x-y$ plane both indicate that the reflection is concentrated toward the z-axis of designed splitter, as presented in Figure 3e,f. The beam splitter can realize various wavefront modulation when different polarization states are input. Therefore, this beam splitter can realize input-polarization multiplexing. Because of broadband circular polarization conversion of structure 1, the multiplexed beam splitter has wide-band operating characteristics at the same time.

In order to realize multifunctional and multiplexed beam splitter which is highly expected for practical applications, we demonstrate a 3D integrated metamaterial by considering input and output optical properties simultaneously. Here, the above-mentioned beam splitter is vertically stacked with a filter metamaterial, as schematically shown in Figure 4a. The bottom layer is the designed broadband beam splitter with polarization

https://dx.doi.org/10.1021/acs.nanolett.0c04795
Nano Lett. XXXX, XXX, XXX−XXX

multiplexing. The top layer is a filter metamaterial with circular hole arrays of different diameters on silver film, which can achieve the transmission of incident lights at different wavelengths. The arrangement of top filter metamaterial is determined by the deflection direction of bottom beam splitter. The operation principle of the 3D integrated metamaterial device is as follows. When RCP light passes vertically through the window in the center of the top metamaterial to bottom beam splitter, the copolarized (RCP) component is vertically reflected from the top window, while the cross-polarized (LCP) component follows the generalized Snell's law and is anomalously deflected. Then, the anomalously deflected cross-polarized light reaches the filtering metamaterial, subsequently leading to the separation of cross-polarized light by space and wavelength. In other words, this 3D integrated metamaterial can be regarded as a miniaturized prism with circular polarization conversion functionality. Compared with previous metasurface-based beam splitters,[26] this 3D integrated beam splitter can further realize the separation of wavelengths for output lights. Therefore, the introduction of a filter makes the broadband beam splitter realize multidimensional control under RCP incidence, including output wavelength, output polarization, and output angle.

The top layer consists of a series of circular hole arrays with different geometric parameters. We assume the thickness of the silver film as 100 nm, and the transmission spectra of the filter metamaterials with different radii and different periods are plotted in Figure 4b. When the anomalously reflected light reaches the top metamaterial, there is an angle between the incident direction and the normal of the top filter. The corresponding angle is in the range of 12°−18.2° for the incident wavelength of 500−750 nm (see Supporting Information). Therefore, the incident angle is approximately set to 15° to reduce the influence of the incident angle on the simulation results. It can be seen that the transmission peaks at different wavelengths can be obtained by adjusting the geometric parameters of periods (P) and radii. It is worth noting that the smaller the radius of the circular hole is, the sharper the transmission peak shows. Therefore, a circular hole array with a smaller radius is purposely selected to achieve effective filtering in the design of 3D integrated metamaterials.

In order to verify the multidimensional control of this 3D integrated metamaterial, we simulate its electric field distributions based on FDTD solutions software. The hole arrays with different periods (P) and radii (R) of filter metamaterial are arranged according to Figure 4a: top array with P = 400 nm, R = 70 nm, right array with P = 450 nm, R = 90 nm, bottom array with P = 550 nm, R = 90 nm, and left array with P = 600 nm, R = 100 nm. The area of each hole array is about 10 μm. Figure 4c shows the simulated electric field distributions in the $x-y$ plane for 3D integrated metamaterial under RCP incidence with different wavelengths. When the incident wavelengths are 529, 569, 635, and 675 nm, respectively, the reflected electric field is mainly accumulated at top, right, bottom, and left of the proposed 3D metamaterial, respectively, as illustrated in Figure 4c. Because of the influence of incident angle on the filtering metamaterial, the wavelength corresponding to the strongest electric field distribution is slightly shifted from that corresponding to the transmission peak in Figure 4b. By varying the areas of hole arrays with different parameters, the intensity ratio among different output beams can be tuned. The electric field distributions indicate that the proposed 3D integrated metamaterials can achieve the separation of cross-polarized light in space and wavelength, thus realizing output-wavelength control and output-angle control simultaneously. When the incident light is switched to linearly polarized light, broadband RCP reflected light can be obtained at the center of the 3D integrated metamaterial, and single-wavelength LCP light flows outward. Therefore, the 3D integrated metamaterial can also operate as a single-wavelength quarter-wave plate under linearly polarized incidence. Moreover, it is more desirable in integrated optical systems compared to conventional bulky quarter-wave plate. In conclusion, this 3D integrated beam splitter could be regarded as a miniaturized prism with polarization conversion functionality, which can generate circularly polarized light with multiple wavelengths simultaneously.

We believe that the proposed metamaterials could be fabricated by the combination of electron beam lithography (EBL) and ion beam etching (IBE) techniques. First, a silver film with a thickness of 100 nm can be deposited on a quartz substrate. Subsequently, ZnO and Ag films are alternately deposited. Then, the multilayered Ag−ZnO film can be exposed by EBL technique to form the designed arrays. In the next step, the designed pattern can be transferred to the Ag−ZnO multilayered film by IBE technique. For the designed 3D integrated beam splitter, the gold marks should be formed by lithography technique after the bottom beam splitter is fabricated. Then, the spacer between the bottom splitter and top filter, which should be transparent in the operating waveband, can be fabricated by film deposition methods. Finally, a 100 nm Ag film can be deposited and then exposed by an overlay EBL process to define the circular hole arrays.

CONCLUSION

In conclusion, a ZnO−Ag-stacked HMM is proposed to realize a multidimensionally controllable switching image and beam splitter in the visible range. Because of various conversion performances of HMMs, the switchable image can be controlled by incident wavelength and reflection polarization simultaneously, thus realizing two optical-parameter controlled image encryption. By introducing the geometric phase arrangement to HMM subunit with broadband circular polarization conversion, a broadband beam splitter with polarization multiplexing is demonstrated. Furthermore, by vertically stacking a filter metamaterial with the broadband beam splitter, a multidimensional metamaterial is demonstrated as a miniaturized prism with polarization conversion functionality. These multidimensional metamaterials offer avenues for the design of multifunctional optical devices and more inspiring possibilities of metamaterials in the future.

ASSOCIATED CONTENT

Supporting Information

The Supporting Information is available free of charge at https://pubs.acs.org/doi/10.1021/acs.nanolett.0c04795.

Electric-field distributions of HMM, influence of incident angle, reflection spectra and PCR spectra of HMMs with different geometric parameters, definitions and calculations of c (contrast) and CCR, calculation of the angles for anomalous reflection, and arrangement of beam splitter (PDF)

https://dx.doi.org/10.1021/acs.nanolett.0c04795
Nano Lett. XXXX, XXX, XXX−XXX

AUTHOR INFORMATION

Corresponding Author

Changzhi Gu − *Beijing National Laboratory for Condensed Matter Physics, Institute of Physics, Chinese Academy of Sciences, Beijing 100190, China; School of Physical Sciences, CAS Key Laboratory of Vacuum Physics, University of Chinese Academy of Sciences, Beijing 100049, China;* orcid.org/0000-0002-2689-2807; Email: czgu@iphy.ac.cn

Authors

Sha Hu − *Beijing National Laboratory for Condensed Matter Physics, Institute of Physics, Chinese Academy of Sciences, Beijing 100190, China; School of Physical Sciences, CAS Key Laboratory of Vacuum Physics, University of Chinese Academy of Sciences, Beijing 100049, China; School of Sciences, Henan University of Technology, Zhengzhou, Henan 450001, China;* orcid.org/0000-0002-3851-8003

Shuo Du − *Beijing National Laboratory for Condensed Matter Physics, Institute of Physics, Chinese Academy of Sciences, Beijing 100190, China; School of Physical Sciences, CAS Key Laboratory of Vacuum Physics, University of Chinese Academy of Sciences, Beijing 100049, China*

Junjie Li − *Beijing National Laboratory for Condensed Matter Physics, Institute of Physics, Chinese Academy of Sciences, Beijing 100190, China; School of Physical Sciences, CAS Key Laboratory of Vacuum Physics, University of Chinese Academy of Sciences, Beijing 100049, China; Songshan Lake Materials Laboratory, Dongguan, Guangdong 523808, China;* orcid.org/0000-0002-1508-9891

Complete contact information is available at: https://pubs.acs.org/10.1021/acs.nanolett.0c04795

Author Contributions

S.H. and S.D. conceived the idea and conducted the calculations and simulations. S.H. prepared the manuscript. J.L. and C.G. supervised the overall project. All the authors analyzed the data and discussed the results. S.H. and S.D. contributed equally to this work.

Notes

The authors declare no competing financial interest.

ACKNOWLEDGMENTS

This work was supported by the National Key Research and Development Program of China (Grants 2016YFA0200400, 2016YFA0200800, and 2016YFA0300601), National Natural Science Foundation of China (Grants 61888102, 12074420, 11674387, 11974386, and 61905274), Strategic Priority Research Program and Key Research Program of Frontier Sciences of Chinese Academy of Sciences (Grants XDB33000000, XDB28000000, and QYZDJ-SSW-SLH042), and Talent Introduction Fund at Henan University of Technology (Grant 2020BS057).

REFERENCES

(1) Yu, N. F.; Genevet, P.; Kats, M. A.; Aieta, F.; Tetienne, J. P.; Capasso, F.; Gaburro, Z. Light Propagation with Phase Discontinuities: Generalized Laws of Reflection and Refraction. *Science* **2011**, *334* (6054), 333−337.

(2) Headland, D.; Carrasco, E.; Nirantar, S.; Withayachumnankul, W.; Gutruf, P.; Schwarz, J.; Abbott, D.; Bhaskaran, M.; Sriram, S.; Perruisseau-Carrier, J.; Fumeaux, C. Dielectric Resonator Reflectarray as High-Efficiency Nonuniform Terahertz Metasurface. *ACS Photonics* **2016**, *3* (6), 1019−1026.

(3) Liu, L.; Zhang, X.; Kenney, M.; Su, X.; Xu, N.; Ouyang, C.; Shi, Y.; Han, J.; Zhang, W.; Zhang, S. Broadband Metasurfaces with Simultaneous Control of Phase and Amplitude. *Adv. Mater.* **2014**, *26* (29), 5031−5036.

(4) Khorasaninejad, M.; Ambrosio, A.; Kanhaiya, P.; Capasso, F. Broadband and Chiral Binary Dielectric Meta-Holograms. *Science Advances* **2016**, *2* (5), No. e1501258.

(5) Chen, H. T.; Taylor, A. J.; Yu, N. F. A Review of Metasurfaces: Physics and Applications. *Rep. Prog. Phys.* **2016**, *79*, 076401.

(6) Hsiao, H.-H.; Chu, C. H.; Tsai, D. P. Fundamentals and Applications of Metasurfaces. *Small Methods* **2017**, *1* (4), 1600064.

(7) Wen, D.; Yue, F.; Liu, W.; Chen, S.; Chen, X. Geometric Metasurfaces for Ultrathin Optical Devices. *Adv. Opt. Mater.* **2018**, *6* (17), 1800348.

(8) Pancharatnam, S. In Generalized Theory of Interference and Its Applications, *Proceedings of the Indian Academy of Sciences-Section A, India*; Springer: India, 1956; pp 398−417.

(9) Berry, M. V. Quantal Phase Factors Accompanying Adiabatic Changes. *Proceedings of the Royal Society of London. A. Mathematical and Physical Sciences* **1984**, *392* (1802), 45−57.

(10) Bomzon, Z.; Biener, G.; Kleiner, V.; Hasman, E. Space-Variant Pancharatnam-Berry Phase Optical Elements with Computer-Generated Subwavelength Gratings. *Opt. Lett.* **2002**, *27* (13), 1141−1143.

(11) Shaltout, A.; Liu, J.; Shalaev, V. M.; Kildishev, A. V. Optically Active Metasurface with Non-Chiral Plasmonic Nanoantennas. *Nano Lett.* **2014**, *14* (8), 4426−4431.

(12) Huang, K.; Dong, Z.; Mei, S.; Zhang, L.; Liu, Y.; Liu, H.; Zhu, H.; Teng, J.; Luk'yanchuk, B.; Yang, J. K. W.; Qiu, C.-W. Silicon Multi-Meta-Holograms for the Broadband Visible Light. *Laser Photonics Rev.* **2016**, *10* (3), 500−509.

(13) Yue, F.; Wen, D.; Xin, J.; Gerardot, B. D.; Li, J.; Chen, X. Vector Vortex Beam Generation with a Single Plasmonic Metasurface. *ACS Photonics* **2016**, *3* (9), 1558−1563.

(14) Fan, R. H.; Xiong, B.; Peng, R. W.; Wang, M. Constructing Metastructures with Broadband Electromagnetic Functionality. *Adv. Mater.* **2019**, *32* (27), 1904646.

(15) Yin, X.; Zhu, H.; Guo, H.; Deng, M.; Xu, T.; Gong, Z.; Li, X.; Hang, Z. H.; Wu, C.; Li, H.; Chen, S.; Zhou, L.; Chen, L. Hyperbolic Metamaterial Devices for Wavefront Manipulation. *Laser Photonics Rev.* **2019**, *13* (1), 1800081.

(16) Li, H.; Hao, W.; Yin, X.; Chen, S.; Chen, L. Broadband Generation of Airy Beams with Hyperbolic Metamaterials. *Adv. Opt. Mater.* **2019**, *7* (20), 1900493.

(17) Groever, B.; Chen, W. T.; Capasso, F. Meta-Lens Doublet in the Visible Region. *Nano Lett.* **2017**, *17* (8), 4902−4907.

(18) Zhou, Y.; Kravchenko, II; Wang, H.; Nolen, J. R.; Gu, G.; Valentine, J. Multilayer Noninteracting Dielectric Metasurfaces for Multiwavelength Metaoptics. *Nano Lett.* **2018**, *18* (12), 7529−7537.

(19) Ye, W.; Zeuner, F.; Li, X.; Reineke, B.; He, S.; Qiu, C.-W.; Liu, J.; Wang, Y.; Zhang, S.; Zentgraf, T. Spin and Wavelength Multiplexed Nonlinear Metasurface Holography. *Nat. Commun.* **2016**, *7*, 11930.

(20) Wen, D.; Yue, F.; Li, G.; Zheng, G.; Chan, K.; Chen, S.; Chen, M.; Li, K. F.; Wong, P. W. H.; Cheah, K. W.; Yue Bun Pun, E.; Zhang, S.; Chen, X. Helicity Multiplexed Broadband Metasurface Holograms. *Nat. Commun.* **2015**, *6*, 8241.

(21) Gao, Y.-J.; Xiong, X.; Wang, Z.; Chen, F.; Peng, R.-W.; Wang, M. Simultaneous Generation of Arbitrary Assembly of Polarization States with Geometrical-Scaling-Induced Phase Modulation. *Phys. Rev. X* **2020**, *10* (3), 031035.

(22) Hu, Y.; Luo, X.; Chen, Y.; Liu, Q.; Li, X.; Wang, Y.; Liu, N.; Duan, H. 3d-Integrated Metasurfaces for Full-Colour Holography. *Light: Sci. Appl.* **2019**, *8*, 86.

(23) Lim, K. T. P.; Liu, H.; Liu, Y.; Yang, J. K. W. Holographic Colour Prints for Enhanced Optical Security by Combined Phase and Amplitude Control. *Nat. Commun.* **2019**, *10*, 25.

(24) Bao, Y.; Yu, Y.; Xu, H.; Guo, C.; Li, J.; Sun, S.; Zhou, Z. K.; Qiu, C. W.; Wang, X. H. Full-Colour Nanoprint-Hologram Synchronous Metasurface with Arbitrary Hue-Saturation-Brightness Control. *Light: Sci. Appl.* **2019**, *8*, 95.
(25) Yin, Z.; Chen, F.; Zhu, L.; Guo, K.; Shen, F.; Zhou, Q.; Guo, Z. High-Efficiency Dielectric Metasurfaces for Simultaneously Engineering Polarization and Wavefront. *J. Mater. Chem. C* **2018**, *6*, 6354−6359.
(26) Zhang, X.; Deng, R.; Yang, F.; Jiang, C.; Xu, S.; Li, M. Metasurface-Based Ultrathin Beam Splitter with Variable Split Angle and Power Distribution. *ACS Photonics* **2018**, *5* (8), 2997−3002.

https://dx.doi.org/10.1021/acs.nanolett.0c04795
Nano Lett. XXXX, XXX, XXX−XXX